Bioactive Materials 6 (2021) 1468–1478

Contents lists available at ScienceDirect

Bioactive Materials

journal homepage: www.sciencedirect.com/journal/bioactive-materials

Investigating the stress corrosion cracking of a biodegradable Zn-0.8 wt%Li alloy in simulated body fluid

Guan-Nan Li [a], Su-Ming Zhu [b], Jian-Feng Nie [b], Yufeng Zheng [a,c,*], Zhili Sun [d,**]

[a] Department of Materials Science and Engineering, College of Engineering, Peking University, Beijing, 100871, China
[b] Department of Materials Science and Engineering, Monash University, Clayton, Australia
[c] International Research Organization for Advanced Science and Technology, Kumamoto University, 2-39-1 Kurokami, Chuo-Ku, Kumamoto, 860-8555, Japan
[d] State Key Laboratory for Turbulence and Complex System, College of Engineering, Peking University, Beijing, 100871, China

ARTICLE INFO

Keywords:
Biodegradable metals
Zn-0.8 wt%Li alloy
Stress corrosion
Slow strain rate testing
Constant-load immersion test

ABSTRACT

Stress corrosion cracking (SCC) may lead to brittle, unexpected failure of medical devices. However, available researches are limited to Mg-based biodegradable metals (BM) and pure Zn. The stress corrosion behaviors of newly-developed Zn alloys remain unclear. In the present work, we conducted slow strain rate testing (SSRT) and constant-load immersion test on a promising Zn-0.8 wt%Li alloy in order to investigate its SCC susceptibility and examine its feasibility as BM with pure Zn as control group. We observed that Zn-0.8 wt%Li alloy exhibited low SCC susceptibility. This was attributed to variations in microstructure and deformation mechanism after alloying with Li. In addition, both pure Zn and Zn-0.8 wt%Li alloy did not fracture over a period of 28 days during constant-load immersion test. The magnitude of applied stress was close to physiological condition and thus, we proved the feasibility of both materials as BM.

1. Introduction

Zn-based materials are considered as promising candidates of BM and have been widely studied over past few years [1–6]. They are prevalent due to their moderate biodegradability and acceptable biocompatibility [7–14]. From a manufacturing point of view, Zn alloys have low melting temperature and good castability [15]. Thus, fabricating and processing Zn alloys normally cost less and consumes lower energy [16].

Zn–Li alloys possess excellent mechanical properties which vary with Li amount and processing methods. Thus, these alloys are favorable as raw materials for load-bearing devices and are intensively studied [17–23]. Zhao et al. investigated hot-rolled Zn-xLi alloy (x = 0.2, 0.4, 0.7 wt%) and claimed that addition of Li to over 0.4 wt% led to decrease in ductility [17]. However, later work by Li et al. proved that hot-warm rolled Zn-0.8 wt%Li alloy had excellent strength and ductility (elongation-to-failure of about 80%) [18]. Further addition of Mg to Zn-0.8 wt% Li alloy gave the highest tensile strength reported so far (Zn-0.8 wt% Li-0.4 wt%Mg alloy with an ultimate tensile strength of 646.69 ± 12.79 MPa) [24].

However, it is worth noticing that for biodegradable applications, high tensile strength alone is not sufficient [25]. Strong interactions between stress and corrosion of the materials in physiological microenvironment may lead to premature, brittle fracture. According to previous researches, formation of micro cracks and a decrease in time to failure by approximately 25% were observed for pure Zn tested in simulated body fluid [26]. At current status, researchers believe that pure Zn is not very sensitive to SCC in physiological environments, while little is known regarding the SCC susceptibility of biodegradable Zn alloys. Previous researches have shown that Zn–Li alloys (Zn-xLi alloy, x = 0.1, 0.4, 0.8 wt%) possessed much higher corrosion rates compared with that of pure Zn during in vitro immersion tests [24]. Also, localized corrosion pits were observed on sample surfaces of Zn-0.8 wt%Li alloy [24]. These results indicated more severe localized corrosion of Zn–Li alloys compared with pure Zn. Under mechanical loading, stress concentration at these pits may induce active dislocation motion and enhance crack propagation by continuously providing fresh substrate that undergoes anodic dissolution.

Hence, this research is aimed at unveiling the interactions between stress and corrosion for a promising Zn-0.8 wt%Li alloy. SSRT was conducted for examining the SCC susceptibility. Simultaneously, self-made loading devices were used for constant-load immersion test to

* Corresponding author. Department of Materials Science and Engineering, College of Engineering, Peking University, Beijing, 100871, China.
** Corresponding author.
E-mail addresses: yfzheng@pku.edu.cn (Y. Zheng), sunzhl@pku.edu.cn (Z. Sun).

https://doi.org/10.1016/j.bioactmat.2020.10.009
Received 17 September 2020; Received in revised form 14 October 2020; Accepted 14 October 2020

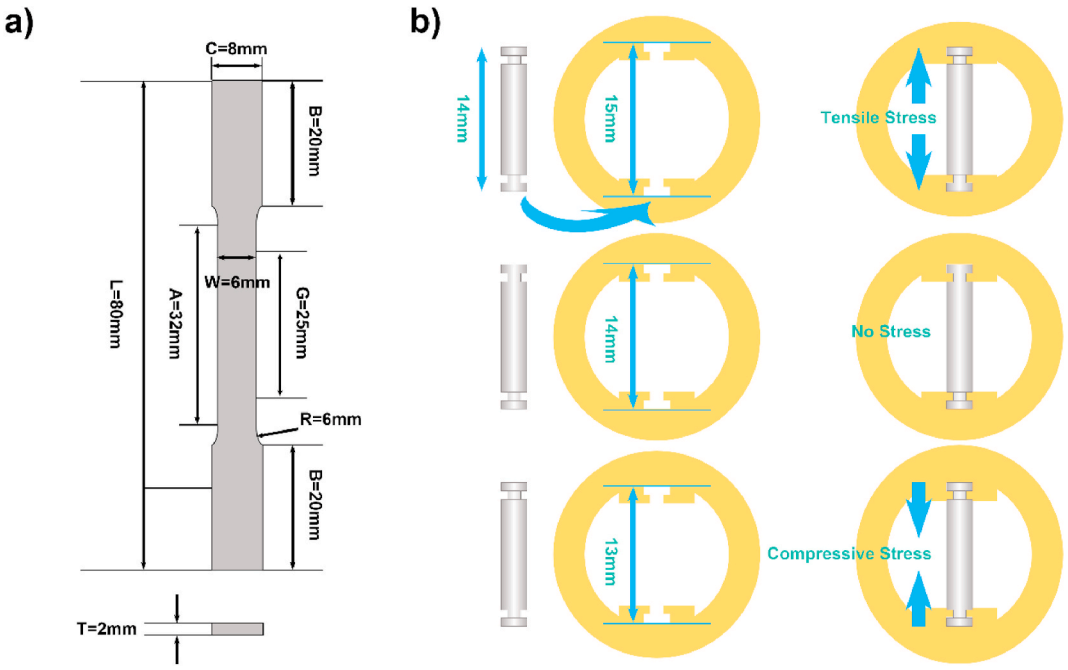

Fig. 1. Metallic samples and PEEK rings used in SSRT and constant-load immersion tests: a) dog-bone samples used for SSRT (gauge length G = 25 mm, width W = 6 mm, thickness T = 2 mm, Radius of fillet R = 6 mm, overall length L = 80 mm, length of reduced section A = 32 mm, length of grip section B = 20 mm, width of grip section C = 8 mm); b) cylindrical samples and PEEK rings designed for constant-load immersion test.

simulate the service condition and examine the feasibility of Zn-0.8 wt% Li alloy as BM.

2. Materials and methods

2.1. Materials and sample preparation

As-cast pure Zn (99.9 wt%) ingots were purchased from Jinzhou Kunteng Nonferrous Metal Materials Technology Co. Ltd., China (hereafter denoted as pure Zn). As-cast Zn-0.8 wt%Li alloy ingots were fabricated by Rare Earth and Alloy Research Institute, Hunan Province, China (hereafter denoted as Zn-0.8 wt%Li alloy). Non-vacuum intermediate frequency melting furnaces and graphite crucibles were applied to prepare alloys. First, the metal Li with a purity of 99.95 wt% and Zn with a purity of 99.99 wt% were made into a Zn-5wt% Li master alloy. Then, the Zn-5wt% Li master alloy was added to the molten Zn solution, and the temperature was kept at about 550 °C for 8 min before casting. Pure Zn and Zn-0.8 wt%Li alloy ingots were then heated to 200 °C, held for 10 min and extruded at the same temperature with an extrusion ratio of 16:1. As-extruded rods with a diameter of 10 mm were cooled in air and fabricated into samples as described in Fig. 1.

2.2. Microstructure characterization

2.2.1. Electron backscatter diffraction (EBSD) analysis

EBSD analysis were conducted on scanning electron microscopy (SEM, JEOL 7001 FEG), coupled with electron backscatter diffraction (EBSD, Aztec analysis system). The EBSD samples were prepared by electro-polishing in a solution containing 33 vol% orthophosphoric acid and 67 vol% ethanol at room temperature and a voltage of 5 V. Data were analyzed using HKL Channel 5 software.

2.2.2. X-ray diffraction (XRD) analysis

XRD analysis was conducted on high-energy X-ray diffractor (SmartLab, Rigaku) with a scanning speed of 20°/min. Samples were mechanically grinded to 2000 grit before analysis. Raw data were collected and phase identification was conducted using MDI JADE 6.5.

Table 1
SSRT results of pure Zn and Zn-0.8 wt%Li alloy in air at room temperature and in circulating SBF at 37 °C.

Materials	Yield Strength (MPa)	Ultimate Tensile Strength (MPa)	Elongation to Failure (%)
Pure Zn (Air)	29.5 ± 2.9	75.6 ± 4.0	46.8 ± 5.0
Zn-0.8 wt%Li alloy (Air)	161.8 ± 7.6	272.7 ± 9.5	146.9 ± 16.4
Pure Zn (SBF)	25.3 ± 0.5	64.8 ± 2.0	36.9 ± 9.4
Zn-0.8 wt%Li alloy (SBF)	133.6 ± 8.3	210.3 ± 5.0	139.5 ± 14.1

2.3. SSRT

2.3.1. SSRT setup

SSRT were conducted on a universal testing machine (Instron 5969) at an initial strain rate of 10^{-5}/s in air at room temperature (RT) and in circulating SBF at 37 °C. Dog-bone shaped specimens with a gauge length of 25 mm, a width of 6 mm and a thickness of 2 mm were machined from extruded bars with the tensile axis parallel to the extrusion direction, as shown in Fig. 1b. Tensile samples were mechanically polished to 5000 grit prior to testing in order to eliminate surface defects.

2.3.2. I_{SCC}

The SCC susceptibility can be evaluated in terms of susceptibility index (I_{SCC}) [27]:

$$I_{SCC}\,(\mathrm{El}) = (\mathrm{El}_{Air} - \mathrm{El}_{SBF})/\,\mathrm{El}_{Air} \quad (1)$$

where El_{Air} and El_{SBF} are the elongations to failure measured at the end of the tests in air and in SBF respectively. I_{SCC} can also be calculated according to ultimate tensile strength (UTS) data [27]:

$$I_{SCC}\,(\mathrm{UTS}) = (\mathrm{UTS}_{Air} - \mathrm{UTS}_{SBF})/\,\mathrm{UTS}_{Air} \quad (2)$$

where UTS_{Air} and UTS_{SBF} are the UTS values measured during the tests in air and in SBF respectively. The El and UTS data in Table 1 were used for

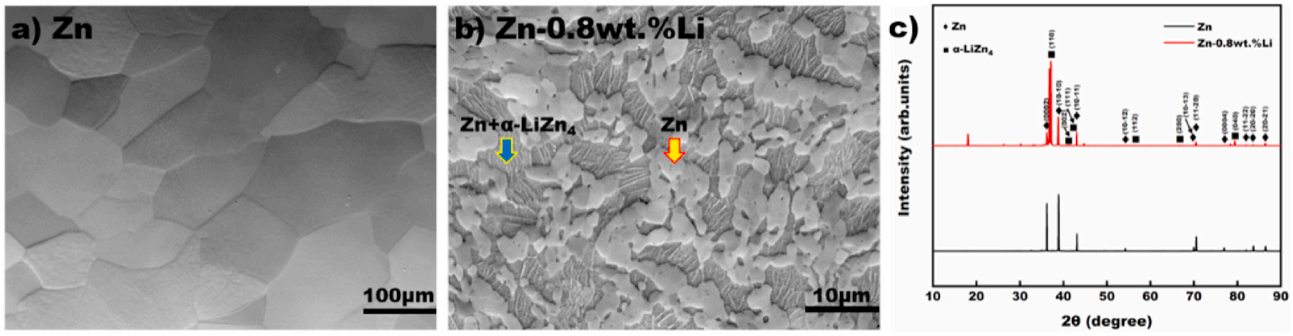

Fig. 2. Microstructure and XRD results of pure Zn and Zn-0.8 wt%Li alloy: SEM images of a) pure Zn and b) Zn-0.8 wt%Li alloy; c) XRD results of pure Zn and Zn-0.8 wt%Li alloy.

generating the I_{SCC} data for these alloys in corrosive media.

2.3.3. Fracture analysis and surface damage analysis

After SSRT, the fractured samples were collected and dried. They were cut from near the fragmented sites, cleaned in absolute ethanol, acetone and observed using SEM (Hitachi S-4800). The morphology at the fracture surfaces and the surface damage near the fracture sites were carefully examined to deduce the fracture mechanism in different environments.

2.4. Constant-load immersion test

2.4.1. Immersion test setup

Cylindrical specimens for immersion test were fabricated according to Fig. 1a. These specimens were ultrasonically cleaned in absolute ethanol and acetone before experiment. Polyether ether ketone (PEEK) rings were designed to provide tensile or compressive stress during immersion. Similar method was proved effective in previous research by Gao et al. [28]. Each metallic specimen was mounted in a PEEK ring by the groove in the specimen and the ring. After installation, the PEEK rings were elastically deformed and thus could apply tensile/compressive stress to the metallic specimens. The magnitudes of the tensile and compressive stress were measured on a universal testing machine (Instron 5969) and calculated to be 11.1 ± 0.2 MPa and 17.7 ± 0.3 MPa respectively. The excellent mechanical property of the PEEK rings guaranteed an enduring stress on metallic specimens without obvious loss after 28 days of immersion (tensile and compressive stress were calculated to be 10.6 ± 0.4 MPa and 18.4 ± 0.2 MPa after 28 days of immersion).

For each kind of materials, fifteen specimens were prepared and cleaned. Five of them were subjected to tensile stress, five of them to compressive stress and the rest of them were not stressed. A ratio of surface area to electrolyte volume of 2.16 mm^2/mL were adopted by placing each specimen in a centrifuge tube containing 45 mL c-SBF (8.035 g/L NaCl, 0.355 g/L $NaHCO_3$, 0.225 g/L KCl, 0.231 g/L $K_2HPO_4{\cdot}3H_2O$, 0.311 g/L $MgCl_2{\cdot}6H_2O$, 0.292 g/L $CaCl_2$, 0.072 g/L NaSO4, 6.118 g/L Tris and suitable HCl) [21] with an initial PH of 7.40. All centrifuge tubes were kept in a 37°C-water bath during the immersion test and the SBF solution was refreshed every 5 days.

2.4.2. Corrosion morphology and corrosion product analysis

After immersion, the specimens were taken out, rinsed by deionized water and dried. Their surface morphology was examined by scanning electron microscope (SEM; Hitachi S-4800). The elemental composition of selected area was investigated using energy-dispersive spectrometer (EDS) at 20 kV accelerating voltage.

In order to evaluate the extent of localized corrosion, cross-section analysis was conducted on the corroded samples. After removal of corrosion products, the samples were mounted in epoxy resin. The mounted samples were then polished until mirror-like surfaces were achieved for SEM observation.

2.4.3. Corrosion rate evaluation

According to ASTM G1-03, corroded specimens were cleaned in hot chromic acid solution (80 °C, 200 g/L CrO_3) for 1 min in order to remove corrosion products. Then, they were rinsed in deionized water, absolute ethanol and dried in open air. Weight loss was measured to calculate the corrosion rate (mm/y) using the following equation:

$$\text{Corrosion Rate} = (K \times W)/(A \times T \times D) \quad (3)$$

where K is a constant (8.76 × 104), T is the time of exposure (h), A is the surface area of the specimen (cm^2), W is the mass loss (g) and D is the density of the material (g/cm^3).

3. Results

3.1. Microstructures of extruded pure Zn and Zn-0.8 wt%Li alloy

The cross-sections of extruded pure Zn and Zn-0.8 wt%Li alloy were examined under SEM. As shown in Fig. 2a, pure Zn exhibited single-phase, recrystallized structure with a certain degree of grain growth [29]. Large grains could reach a size of over 200 μm, while small grains were less than 50 μm. Zn-0.8 wt%Li alloy (Fig. 2b), on the other hand, was composed of two distinct regions: 1) α-$LiZn_4$+Zn eutectoid region with lamellar structures and 2) Zn region consisting of recrystallized grains. This result was in accordance to Li–Zn phase diagram [30]. The $LiZn_4$ phase should be α-$LiZn_4$ instead of β-$LiZn_4$ since the latter is not stable during storage at room temperature [31]. Inside the eutectoid region, lamellar phase with brighter contrast should be Zn and the rest area with darker contrast should be α-$LiZn_4$. Inside eutectoid area, Zn phase had a characteristic thickness of less than 1 μm. Meanwhile, recrystallized Zn grains that distributed evenly throughout the cross-section had a diameter of a few microns.

XRD analysis was conducted to identify the phase composition of these materials. Data analysis confirmed the existence of Zn and α-$LiZn_4$ as shown in Fig. 2c. Published crystal parameters of α-$LiZn_4$ [32] were applied to simulate XRD patterns for comparing with experimental results. Diffraction peak intensities varied from standard patterns due to the strong texture developed after extrusion (as revealed by EBSD results in Fig. 3). For Zn-0.8 wt%Li alloy, diffraction peaks at the 2θ value of about 18° and 30° was hard to explain. These peaks might correspond to oxide composed of Li, Zn and O since no protection gas was adopted during casting of these alloys. Or they might derive from the modulated structure of α-$LiZn_4$ [32].

Further analysis of the extruded microstructure was done by EBSD and corresponding results are shown in Fig. 3 (pure Zn) and Fig. 4 (Zn-0.8 wt%Li alloy). Clearly, the microstructure of extruded pure Zn was composed of large number of small grains and a few very large grains. Data analysis reveals that pure Zn has an average grain size of 39.5 ±

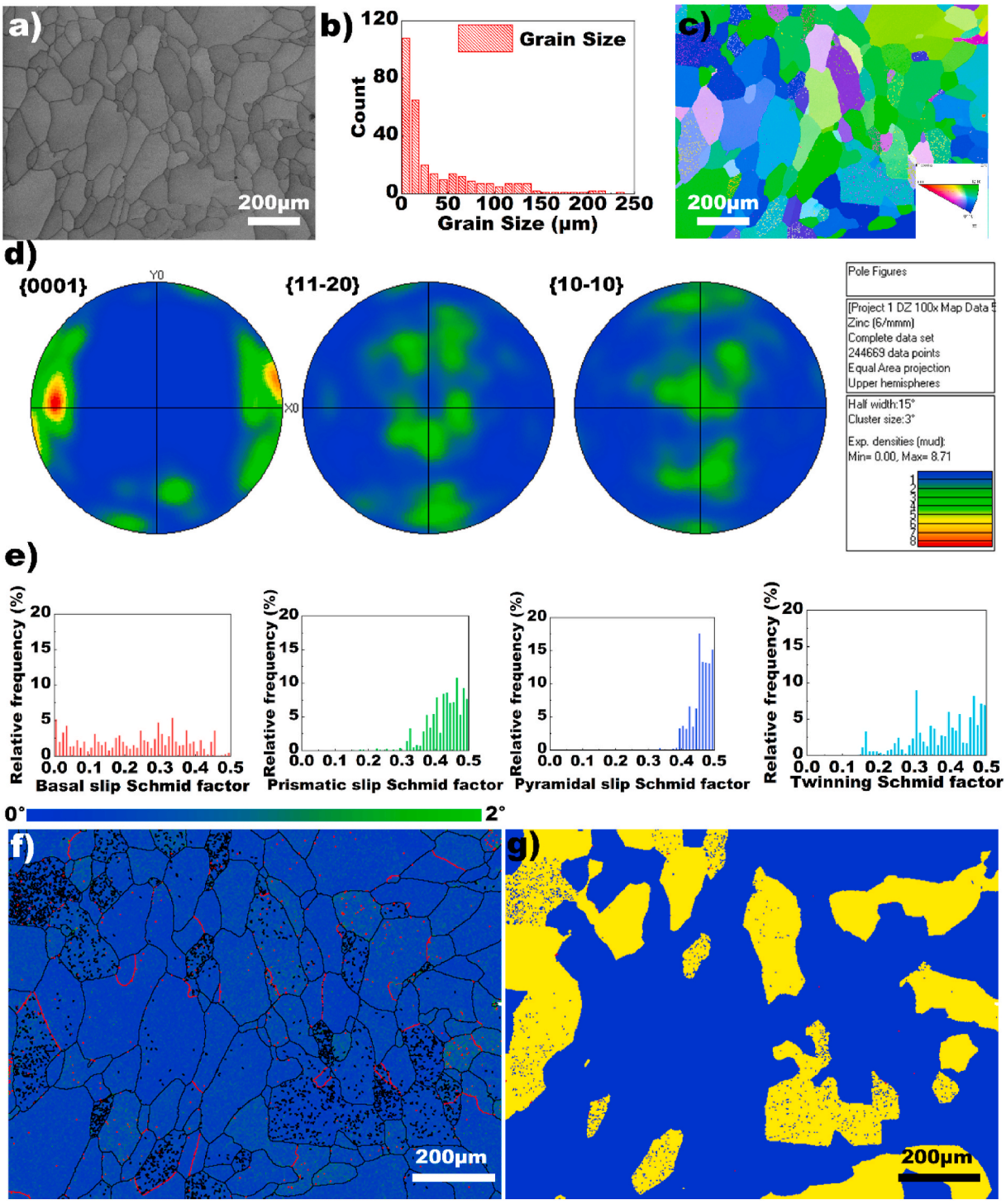

Fig. 3. EBSD measurements of pure Zn after extrusion: a) band contrast map; b) grain size distribution; c) inverse pole figure (IPF) map of Z direction which is parallel to extrusion direction; d) {0001}, {11–20} and {10-10} pole figures; e) Schmid factor distribution of basal slip, prismatic slip, pyramidal <a> slip and {10–12}<10-1-1> deformation twinning; f) Kernel Average Misorientation (KAM) map with color bar corresponding to local misorientation from 0° to 2°; g) recrystallization analysis map where blue represents fully recrystallized region, yellow represents substructure and red represents deformed region.

46.9 μm (304 grains). Large grains could reach a size of ~230 μm while the diameters of small grains are less than 10 μm. IPZ map in Fig. 3c shows that for most grains, <-12-10> and <01–10> directions were aligned parallel to extrusion direction. Also, it can be concluded from pole figures that extruded pure Zn possessed a texture of <0001> direction lying perpendicular to the extrusion direction with a maximum intensity of 8.71. Such an orientation inhibits basal slip and favors <c+a> pyramidal slip during tension along extrusion direction as revealed by Schmid factor calculation in Fig. 3e. For better understanding of dynamic recrystallization that happened during hot extrusion. KAM map and recrystallized fraction were calculated. Several low-angle grain boundaries (red, 2–10°) can be observed amid large number of high-angle grain boundaries (black, >10°). KAM calculation indicates little misorientation inside each grain and suggests a low internal stress state left after processing. This is further confirmed by recrystallization analysis (Fig. 3g) in which blue region represents fully recrystallized

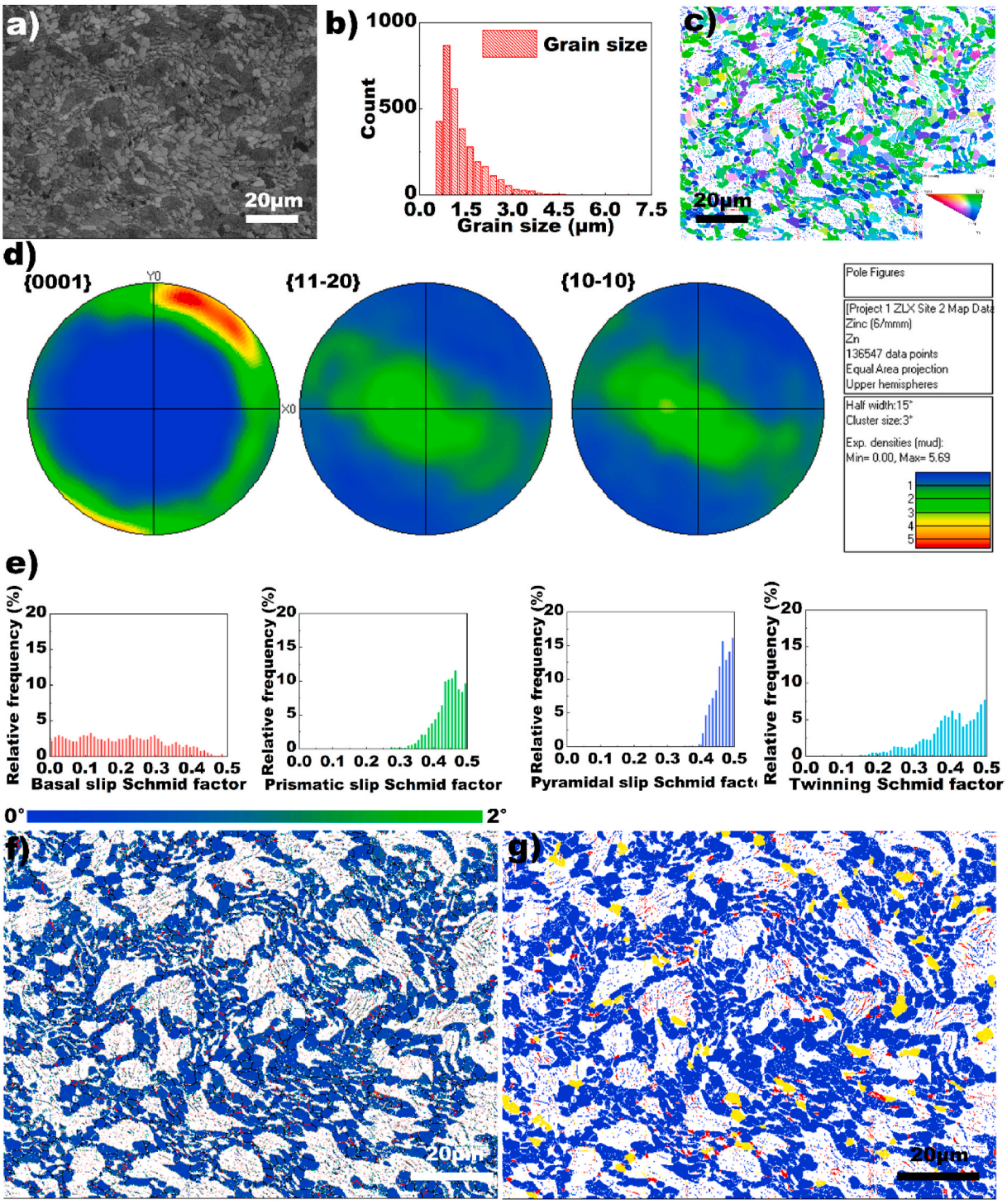

Fig. 4. EBSD measurements of Zn phase in Zn-0.8 wt%Li alloy after extrusion: a) band contrast map; b) grain size distribution; c) inverse pole figure (IPF) map of Z direction which is parallel to extrusion direction; d) {0001}, {11–20} and {10-10} pole figures; e) Schmid factor distribution of basal slip, prismatic slip, pyramidal <a> slip and {10–12}<10-1-1> deformation twinning; f) Kernel Average Misorientation (KAM) map with color bar corresponding to local misorientation from 0° to 2°; g) recrystallization analysis map where blue represents fully recrystallized region, yellow represents substructure and red represents deformed region.

area while yellow region suggests the existence of substructure. Deformed region (colored red) with high stored energy is not observed.

Fig. 4 displays the EBSD results of Zn-0.8 wt%Li which is composed of Zn and α-$LiZn_4$. However, α-$LiZn_4$ was identified as pure Zn phase by the testing instrument due to the similarity of its crystal structure with Zn. The influence of such misidentifications was avoided by removing α-$LiZn_4$ phase from the final results and analyzing merely the Zn phase [31]. The average grain size of Zn grains was 1.4 ± 0.7 μm. According to IPZ map (Fig. 4c) and pole figure (Fig. 4d), Zn-0.8 wt%Li alloy possessed similar texture with pure Zn but with a weaker intensity of 5.69. Compared with pure Zn, Zn-0.8 wt%Li alloy had slightly larger internal stress as elucidated by the KAM map. In addition, deformed structure can be found at the boundaries of recrystallized Zn region and α-$LiZn_4$+Zn eutectoid region. Both KAM map and recrystallization analysis suggest that the eutectoid area retains some deformation stored energy after hot extrusion.

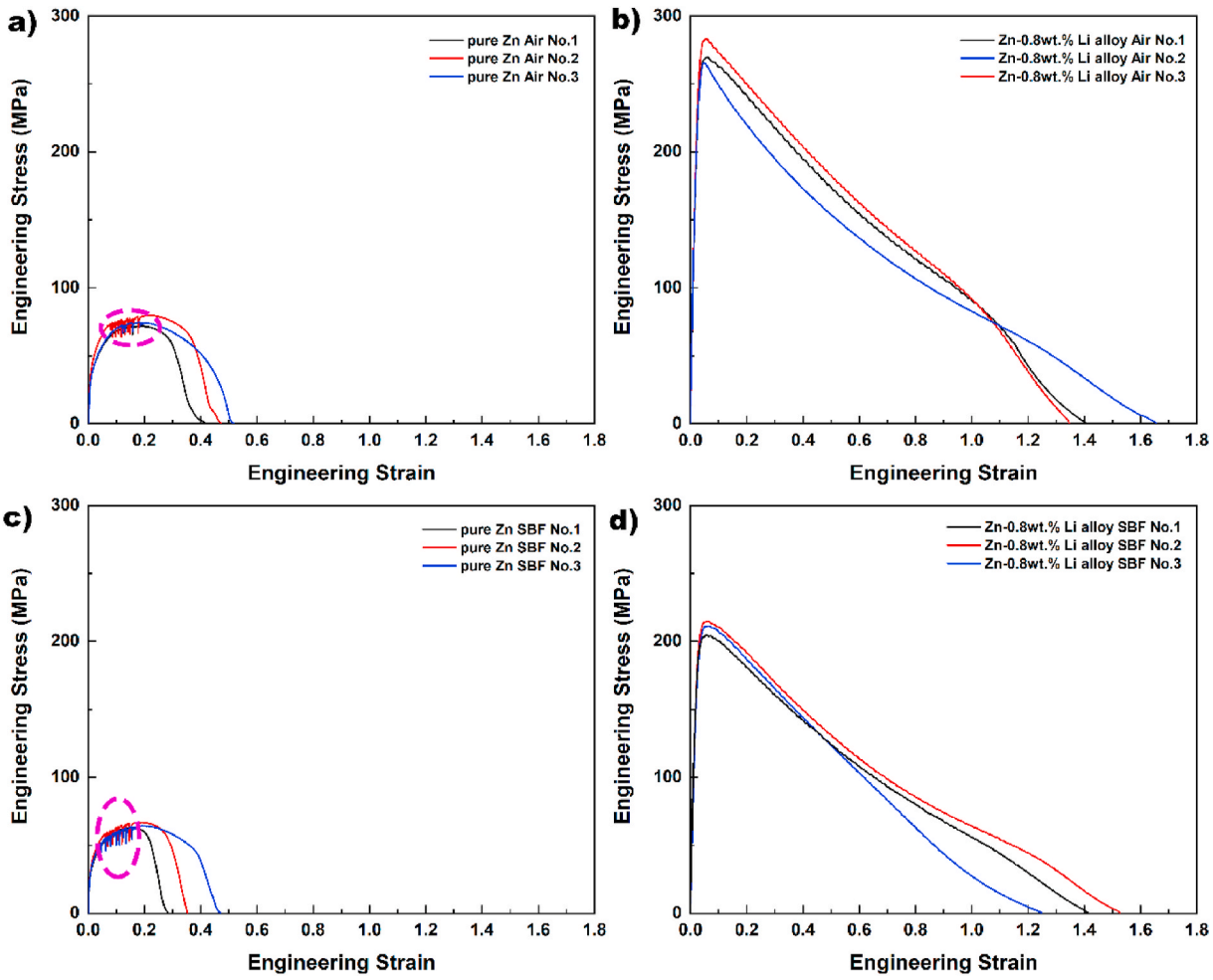

Fig. 5. Engineering stress-strain curves of pure Zn and Zn-0.8 wt%Li alloy: a) pure Zn tested in air at room temperature; b) Zn-0.8 wt%Li alloy tested in air at room temperature; c) pure Zn tested in circulating SBF at 37 °C; d) Zn-0.8 wt%Li alloy tested in circulating SBF at 37 °C.

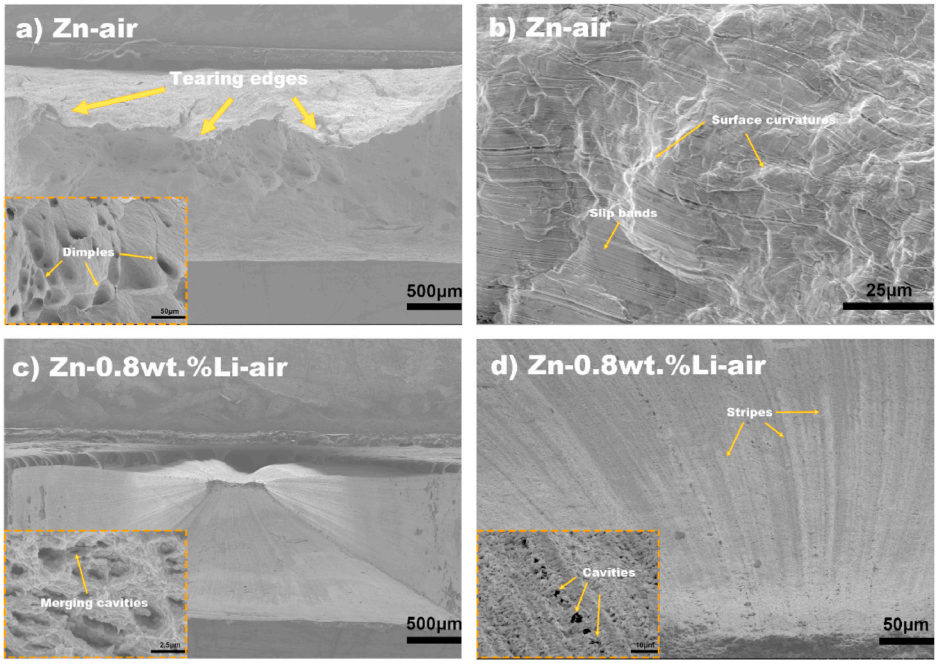

Fig. 6. Fractography and surface damage morphology of pure Zn and Zn-0.8 wt%Li alloy tested in air at room temperature: a) fractography of pure Zn; b) surface damage morphology of pure Zn; c) fractography of Zn-0.8 wt%Li alloy; d) surface damage morphology of Zn-0.8 wt%Li alloy.

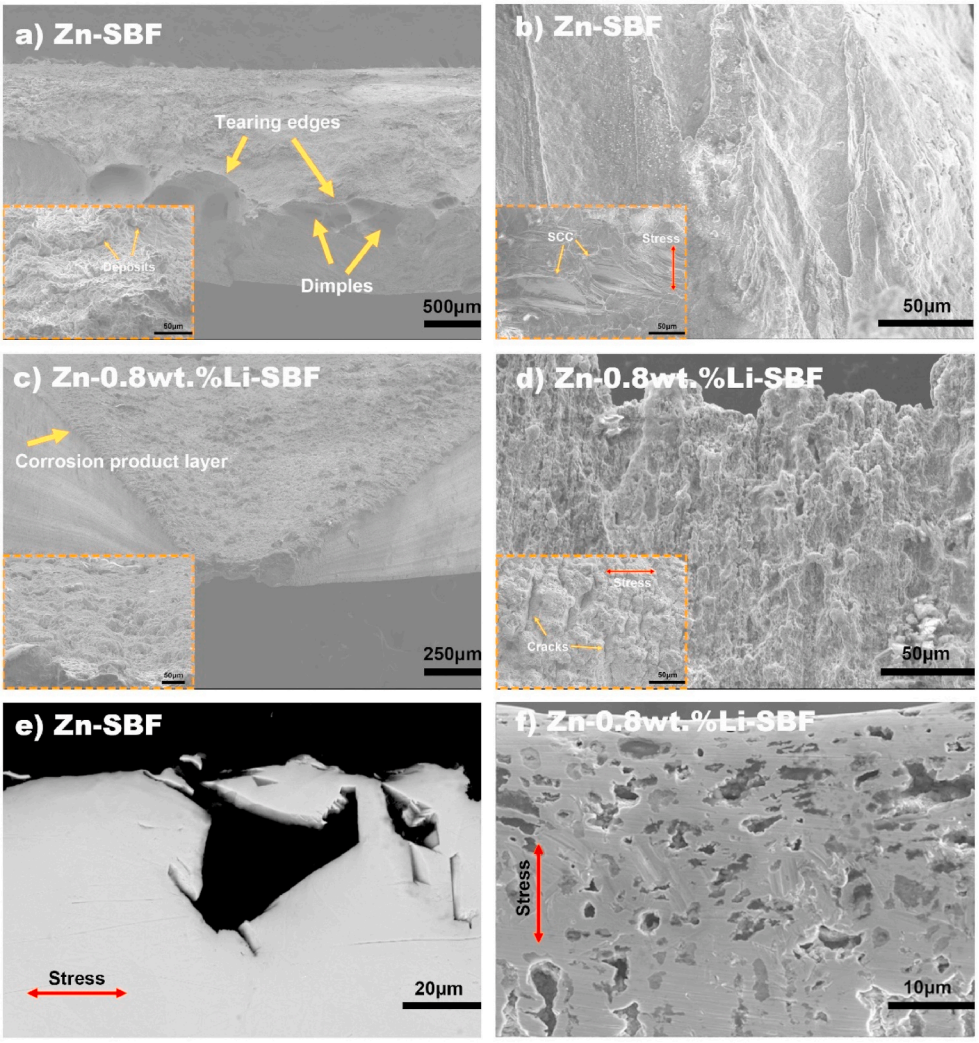

Fig. 7. Fractography, surface damage morphology and longitudinal sections of pure Zn and Zn-0.8 wt%Li alloy tested in circulating c-SBF at 37 °C: a) fractography of pure Zn; b) surface damage morphology of pure Zn; c) fractography of Zn-0.8 wt%Li alloy; d) surface damage morphology of Zn-0.8 wt%Li alloy; e) longitudinal section showing brittle cracks on pure Zn after SSRT in SBF; f) longitudinal section showing cavities containing corrosion products and micro-cracks in Zn-0.8 wt%Li alloy after SSRT in SBF.

3.2. SSRT

3.2.1. Stress-strain curve and I_{SCC}

Engineering stress-strain curves of SSRT are shown in Fig. 5. Mechanical properties of pure Zn, Zn-0.8 wt%Li alloy tested in air and in SBF are presented in Table 1. Pure Zn exhibited relatively low strength and ductility. In engineering stress-strain curve of pure Zn, the strain hardening region was followed by a serrated region which might result from formation of deformation twins [29]. Necking was not prominent for pure Zn and cross-section reduction was limited, as will be shown by fractography. Alloying with Li significantly improved the mechanical properties of pure Zn regarding to strength and ductility. Limited strain hardening range was followed by pronounced necking phenomena indicating that strain was restricted to limited area near fracture end. Such results suggested that Zn-0.8 wt%Li alloy might deform by grain boundary sliding and/or dynamic recrystallization, as had been observed on another Zn–Li alloy [19].

When tested in circulating SBF at 37 °C, both strength and elongation-to-failure decreased compared to the experimental data under ambient condition. Such a trend was confirmed by I_{SCC} values. The loss in strength as a result of exposure to corrosive solution was more obvious for Zn-0.8 wt%Li alloy (I_{SCC} (UTS) = 0.229). The loss in elongation-to-failure, on the other hand, was not prominent for Zn-0.8 wt%Li alloy (I_{SCC} (El) = 0.050).

3.2.2. Fractography and surface damage

Fig. 6 showed the fractography and surface damage morphology of the samples tested in air at room temperature. These figures could help us speculate the deformation and fracture mechanisms of these materials. For pure Zn, the surface was curvy and uneven showing signs of slip and grain rotation. Limited cross-section reduction and large dimples suggested restricted ductility which was probably due to the large grain size of pure Zn. Addition of Li induced effective grain refinement and led to great improvement in mechanical properties. The cross-section reduction was very large for Zn-0.8 wt%Li alloy and the size of dimples at fracture surface decreased to a few microns. Meanwhile, the surface remained rather flat with obvious stripes parallel to the loading direction and protruding cavities near fracture end. These stripes might be the traces of grain boundary sliding and the cavities on them were probably formed at triple junctions during deformation process [33].

Fig. 7 showed the fractography and surface morphology of the samples tested in circulating SBF at 37 °C. Both materials were tested at a strain rate of 10^{-5}/s, and corrosion did not change their intrinsic ductile behaviors at this strain rate. For pure Zn (Fig. 7a–b), dimples and tearing edges could still be seen at fracture ends and cracks were found far away from fracture ends contributing little to the failure of the sample. In terms of Zn-0.8 wt%Li alloy (Fig. 7c–d), corrosion had made it difficult to observe the small dimples at fracture ends, leaving only corrosion morphology at the fracture surfaces. The cracks were shallow in the corrosion product layer and did not seem to attack the metallic substrate. Fig. 7e–f showed the longitudinal section of the materials after

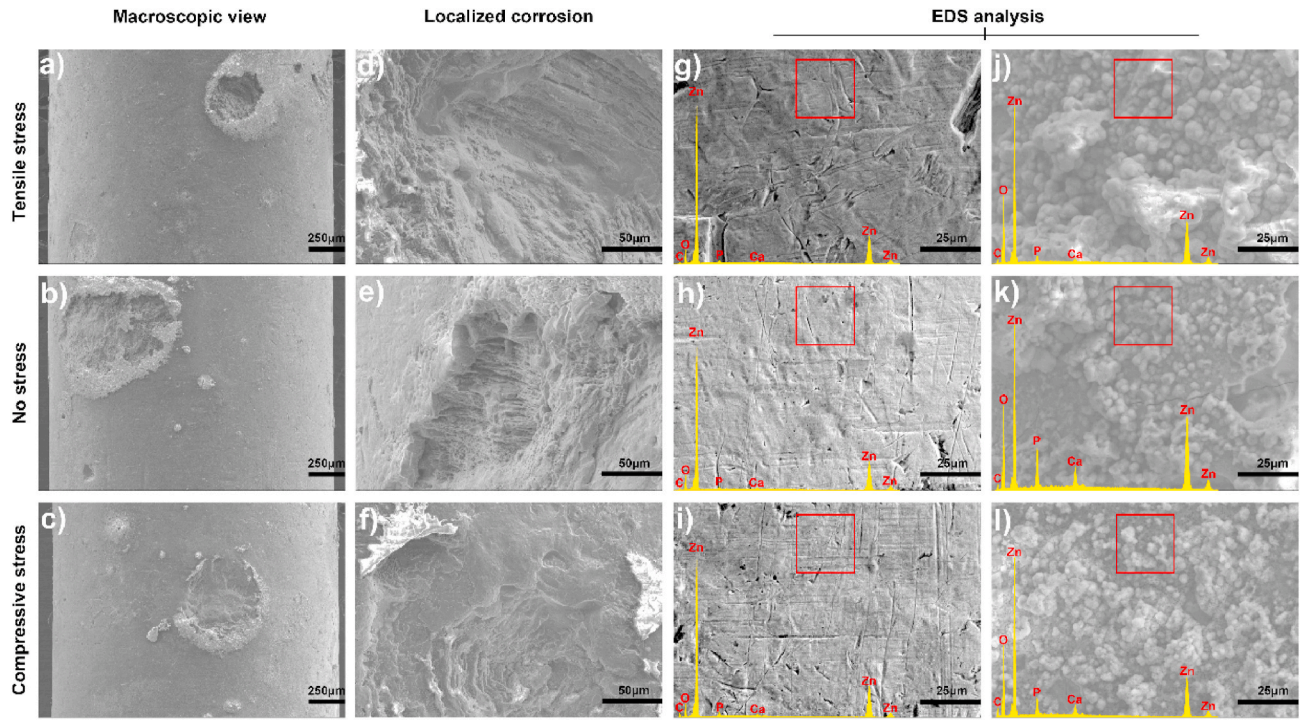

Fig. 8. Surface morphology and selected EDS analysis results of pure Zn after 28 days immersion in SBF under different stress state: a-c) overview of corrosion morphology; d-f) corrosion pits on sample surfaces; g-l) EDS analysis of selected area.

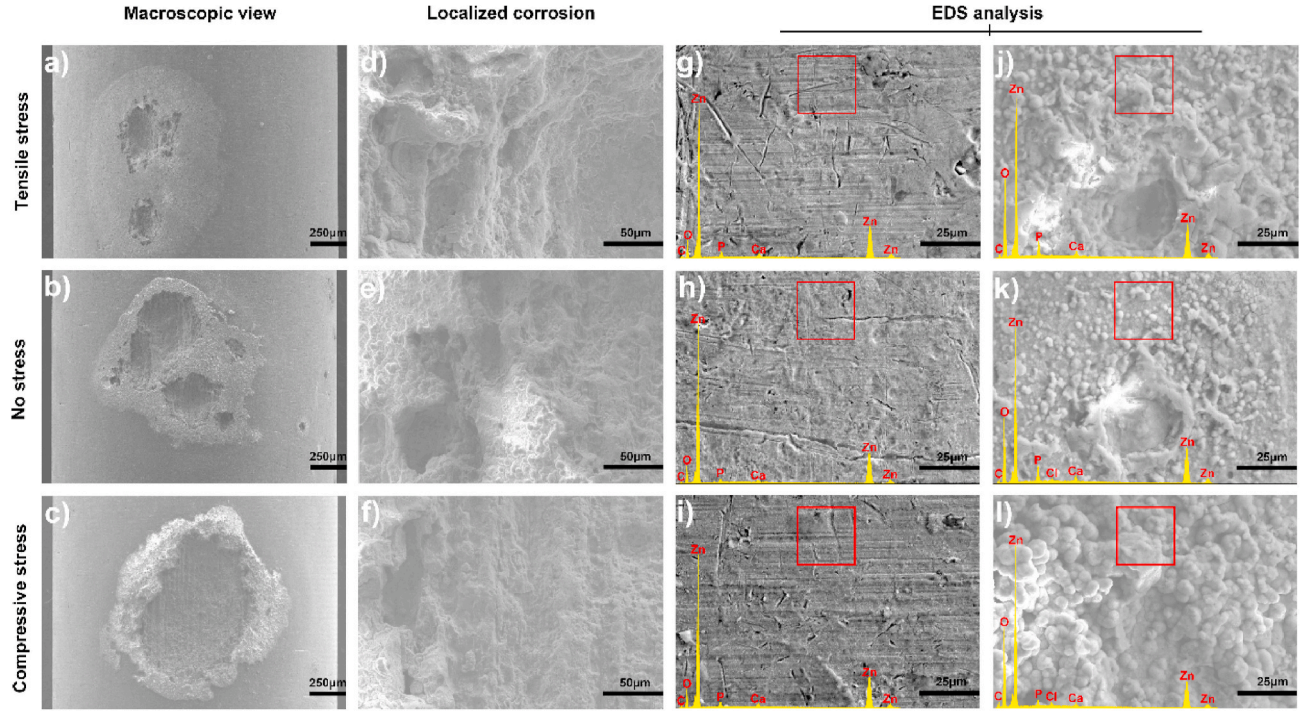

Fig. 9. Surface morphology and selected EDS analysis results of Zn-0.8 wt%Li alloy after 28 days immersion in SBF under different stress state: a-c) overview of corrosion morphology; d-f) corrosion pits on sample surfaces; g-l) EDS analysis of selected area.

SSRT in SBF. The differences were quite obvious. For pure Zn, brittle cracks were observed with a length of about 20 μm. These cracks usually located at corrosion pits which undermined the substrate and provided relatively occluded environments for localized corrosion. On the other hand, Zn-0.8 wt%Li alloy was characterized by cavities filled with corrosion products near fracture end. The cavities formed arrays parallel to the loading direction (as shown in Fig. 6d) and were in touch with corrosive medium by holes at sample surfaces. A few micro-cracks could be found inside the cavities and many large cavities extended perpendicular to the loading direction.

Table 2
wt loss and corrosion rate data measured and calculated after removal of corrosion products. (T: tensile stress; N: no stress; C: compressive stress).

Test groups	Weight Loss (mg)	Corrosion rate (mm/y)
Pure Zn (T)	6.7 ± 0.3	0.127 ± 0.006
Pure Zn (N)	6.2 ± 0.8	0.118 ± 0.016
Pure Zn (C)	6.6 ± 0.7	0.125 ± 0.013
Zn-0.8 wt%Li alloy (T)	6.6 ± 0.9	0.129 ± 0.017
Zn-0.8 wt%Li alloy (N)	6.3 ± 1.2	0.124 ± 0.023
Zn-0.8 wt%Li alloy (C)	6.3 ± 0.3	0.125 ± 0.006

3.3. Constant-load immersion test

3.3.1. Corrosion morphology and corrosion products

Constant-load immersion test provided a strain rate of near zero and simultaneously a stress value close to physiological condition. However, despite the differences in alloying composition and stress state, the corrosion morphology appeared very similar macroscopically, as shown in Fig. 8a–c (pure Zn) and Fig. 9a–c (Zn-0.8 wt%Li alloy). All test groups were characterized by large area of flat and uniform corrosion layer (Fig. 8g–i and Fig. 9g–i) together with some localized corrosion area (Fig. 8d–f and Fig. 9d–f). Mass accumulation of particulate matter could be observed around pitting holes. This corrosion mode seemed unaffected by neither the stress state nor the material composition. EDS analysis of selected area was conducted and the results were displayed in Fig. 8g-l (pure Zn) and Fig. 9g-l (Zn-0.8 wt%Li alloy). Typical areas were selected on uniform corrosion surfaces and near localized corrosion pits. C, O, Zn, Ca and P were detected on both uniform corrosion zones and surface deposits. Small variations between the compositions of these areas could be recognized. Higher Ca, P peaks could be expected for surface deposits. According to EDS results, dense corrosion layer should mainly be composed of ZnO/$Zn(OH)_2$ and some carbonates. Tiny particles dispersed on compact corrosion layer as well as particulate matter that accumulated around the corrosion pits were probably apatite, which explained the higher Ca and P peaks detected. At some of these selected areas with sediments, Cl was detected, which might come from residual chlorine salts.

3.3.2. Corrosion rate evaluation

After removing corrosion products, samples were dried and weighed. The measured weight loss and calculated corrosion rate were presented in Table 2. The corrosion rates of pure Zn and Zn-0.8 wt%Li alloy were close to each other suggesting that Li addition did not significantly change the corrosion behavior of Zn. For both materials, it can be concluded that the corrosion rate is not significantly affected by tensile or compressive stress. This might be due to the fact that the stress applied by the PEEK rings were relatively small and the influence of stress on corrosion was low at this stress level.

4. Discussion

4.1. Stress corrosion behavior of pure Zn and Zn-0.8 wt%Li alloy

The microstructures of pure Zn and Zn-0.8 wt%Li alloy were rather different, as shown in the previous section. Compared to pure Zn, Zn-0.8 wt%Li alloy possessed finer grains with similar texture and an extra Zn+α-$LiZn_4$ eutectoid region. Such a difference caused a variation in deformation mechanism, which also influenced the stress corrosion behavior. By analyzing stress-strain curve and surface damage morphology, it was deduced that large surface curvatures induced by slip/deformation twinning/rotation of large grains during deformation of pure Zn eased the formation of SCCs. For further evidence, the deformed structure near fracture end of pure Zn and Zn-0.8 wt%Li alloy was analyzed by EBSD (Fig. 10). Grains whose <0001> directions were nearly parallel to the extrusion direction (also the tensile direction) could be found in pure Zn. These grains might be deformation twins that grew after nucleation or they might have experienced grain rotations. Anyway, they should be responsible for the curvatures and SCCs observed for pure Zn.

Based on experimental results, we proposed that the dominating mechanism of SCC formation on pure Zn should be slip-anodic dissolution mechanism [34]. A schematic description is displayed in Fig. 11a. For pure Zn, surface curvatures resulting from grain rotation or twin

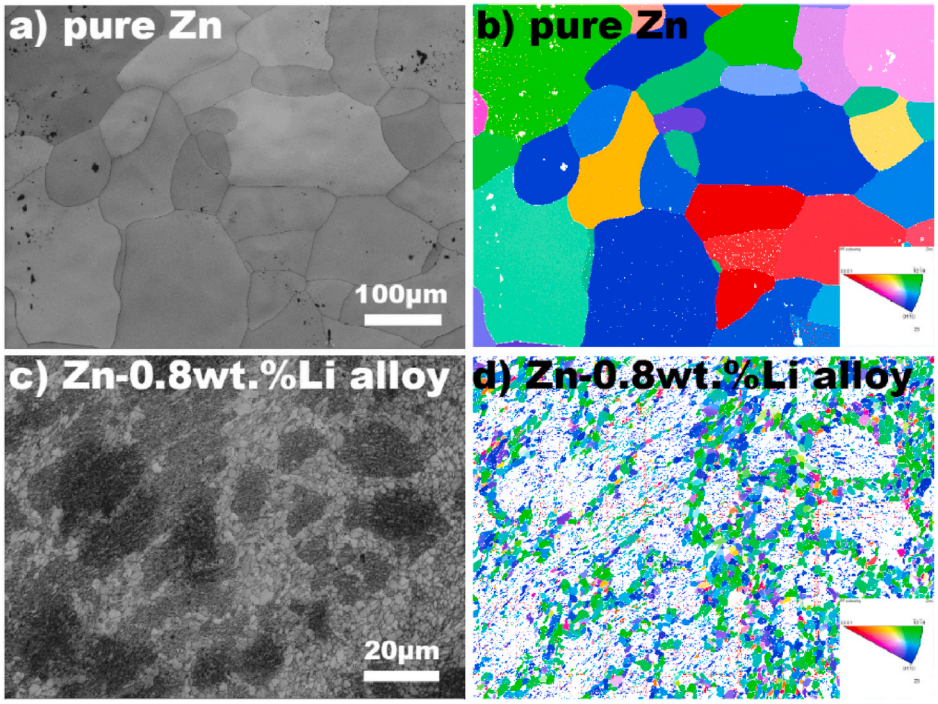

Fig. 10. EBSD results of pure Zn (a and b) and Zn-0.8 wt%Li alloy (c and d) after SSRT: a) and c) band contrast map; b) and d) inverse pole figure (IPF) map of Z direction which is parallel to tensile direction.

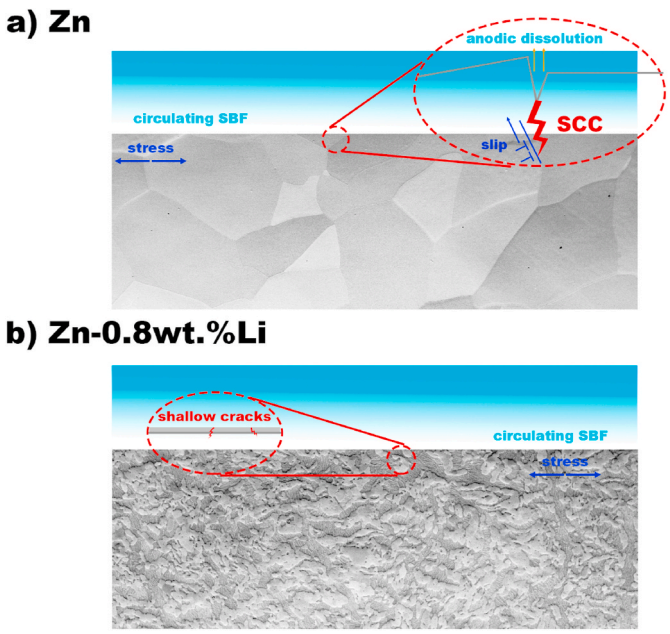

Fig. 11. Proposed mechanism of crack formation on a) pure Zn and b) Zn-0.8 wt%Li alloy.

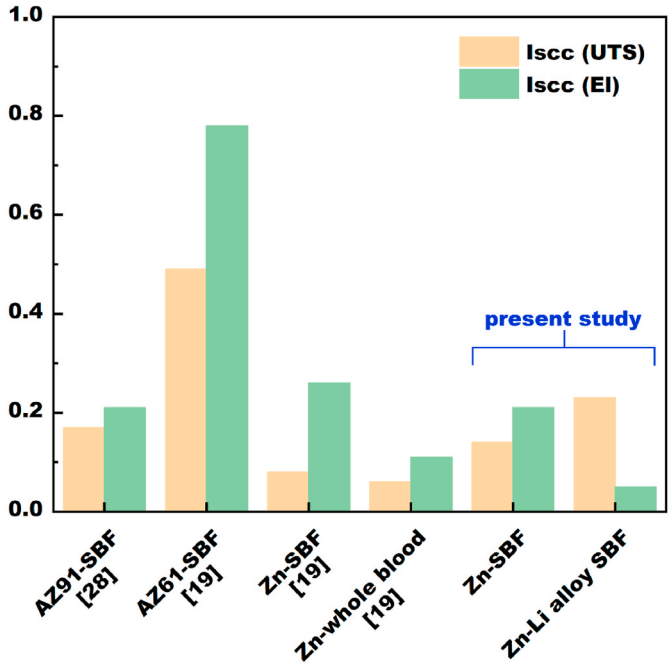

Fig. 12. Comparison of the SCC susceptibility of Mg-based and Zn-based BM investigated by SSRT.

growth provided preferential sites for crack initiation. Dislocation movements were highly activated and fresh surfaces were produced which experienced anodic dissolution leading to formation of micro-cracks. Then stress concentration and dislocation slip near crack tips cause intense anodic dissolution and further growth of the cracks to form SCCs. For Zn-0.8 wt%Li alloy (Fig. 11b), no such curvatures were formed during deformation. The uniform corrosion layer was stressed and shallow cracks could be found. Nevertheless, they were not able to attack deeply into the metallic substrate. Stripes that were parallel to tensile deformation (as shown in Fig. 6) could not be expanded by stress. This explained the very low *Iscc* (El) of Zn-0.8 wt%Li alloy. Surface cavities introduced corrosive medium into the metallic substrate and created a few micro-cracks inside Zn-0.8 wt%Li alloy. This enhanced the cross-section reduction and could explain the prominent decrease in tensile strength.

Generally, materials are subjected to two kinds of stress that may influence their stress corrosion behaviors: internal stress and external stress. Zn-based materials normally have low melting temperatures and are susceptible to dynamic recrystallization during processing [19]. EBSD results have shown that little internal stress is accommodated in dislocation structure after hot extrusion and thus should contribute little to SCC. During fabrication of cylindrical samples for immersion test, surface tension induced by milling might be introduced. Stent fabrication procedures such as laser cutting are capable of creating stress and heat treatment is normally applied for this sake. Characterizations and investigations of such stress state are important for optimizing the fabrication of biodegradable stents.

Considering the external stress involved in SSRT, the applied strain rate may significantly influence the results of the experiment [35]. Earlier studies had shown that Mg alloys are more sensitive when tested at a strain rate of 10^{-7}/s than at 10^{-6}/s [36]. However, no such comparative results were given for Zn alloys. Therefore, a strain rate sensitivity of 10^{-5}/s was applied in current paper for better comparison with previous research data [26]. The observed fracture surfaces confirmed that the fracture was dominated by mechanical failure instead of SCC due to the relatively high strain rate applied in the present research. Lower strain rate is needed to clarify the sensitive region of these materials.

4.2. Comparison of the SCC susceptibility of Zn-based and Mg-based BM

Fig. 12 shows the SCC susceptibility of AZ91 [36], AZ61 and pure Zn [26] extracted from published results. Apparently, Mg alloys possessed higher I_{SCC} than pure Zn and Zn-0.8 wt%Li alloy. This could be attributed to the lower strain rate applied during SSRT of Mg alloys. In addition, it is worth noticing that the SBF applied in the present research was c-SBF, which had 58.0% lower HCO_3^- concentration compared with *m*-SBF [37]. Such large discrepancies might also contribute to the high I_{SCC} observed for AZ61 since SCC formation on Mg alloys has been reported to be sensitive to HCO_3^- [36,38]. It has been concluded that the existence of organic species in whole blood reduced the effect of stress corrosion by covering the material surface with passive film [26,28]. In present study, Zn-0.8 wt%Li alloy was tested in SBF without the existence of any organic species. Thus, even higher SCC resistance can be expected during practical applications.

During constant-load immersion test, although localized corrosion was observed, SCC that stretched perpendicular to loading direction was absent. Moreover, unlike pure Mg, the corrosion rates of pure Zn and Zn-0.8 wt%Li were not significantly accelerated by tensile or compressive stress. This was probably due to the fact that the applied constant stress was lower than the stress required to induce SCC, commonly known as threshold stress (σ_{th}). Larger stress was proved to be capable of inducing significant differences in corrosion rate [39]. However, the stress magnitude chosen in present study was believed to be close to the stress in vivo [28] and was thus sufficient to mimic the service condition. Similar experimental setup caused the fracture of pure Mg samples but did not undermine the mechanical integrity of pure Zn and Zn-0.8 wt%Li alloy. More sustainable mechanical support can thus be provided by Zn-based BM.

5. Conclusions

In the present research, the stress corrosion behaviors of pure Zn and Zn-0.8 wt%Li alloy were investigated using SSRT and constant-load immersion test. Following conclusions were drawn:

1) Alloying with Li resulted in the formation of Zn+α-$LiZn_4$ eutectoid region and significantly refined the grain size of pure Zn. Meanwhile, introducing Li improved both the strength and ductility but shortened the work hardening range of pure Zn.

2) When stressed in SBF, the strength and elongation-to-failure of pure Zn and Zn-0.8 wt%Li alloy decreased. Compared with pure Zn, the strength of Zn-0.8 wt%Li alloy was more sensitive while its elongation-to-failure was less sensitive to the corrosive environment (SBF).

3) After SSRT, SCCs were observed for both materials. However, cracks failed to attack deeply into the metallic substrate of Zn–Li alloy and thus had little influence on elongation-to-failure.

4) Constant load as large as 11.1 ± 0.2 MPa (tensile) and 17.7 ± 0.3 MPa (compressive) did not significantly change the corrosion behaviors of pure Zn and Zn-0.8 wt%Li alloy within a time scale of 28 days.

5) After constant-load immersion test, cracks were not observed but pitting corrosion was obvious. Pure Zn and Zn-0.8 wt%Li alloy did not fracture after 28 days of immersion under tensile or compressive stress.

CRediT authorship contribution statement

Guan-Nan Li: Methodology, Investigation, Formal analysis, Writing - original draft. **Su-Ming Zhu:** Investigation, Resources. **Jian-Feng Nie:** Supervision, Validation, Resources. **Yufeng Zheng:** Conceptualization, Writing - review & editing, Resources, Supervision, Funding acquisition. **Zhili Sun:** Resources, Validation, Supervision.

Declaration of competing interest

None.

Acknowledgement

This work was supported by National Natural Science Foundation of China (Grant No. 51931001).

References

[1] D. Hernandez-Escobar, S. Champagne, H. Yilmazer, B. Dikici, C.J. Boehlert, H. Hermawan, Current status and perspectives of zinc-based absorbable alloys for biomedical applications, Acta Biomater. 97 (2019) 1–22.
[2] Z.Z. Shi, X.X. Gao, H.J. Zhang, X.F. Liu, H.Y. Li, C. Zhou, Y.X. Yin, L.N. Wang, Design biodegradable Zn alloys: second phases and their significant influences on alloy properties, Bioact Mater 5 (2) (2020) 210–218.
[3] D. Vojtech, J. Kubasek, J. Serak, P. Novak, Mechanical and corrosion properties of newly developed biodegradable Zn-based alloys for bone fixation, Acta Biomater. 7 (9) (2011) 3515–3522.
[4] P.K. Bowen, E.R. Shearier, S. Zhao, R.J. Guillory 2nd, F. Zhao, J. Goldman, J. W. Drelich, Biodegradable metals for cardiovascular stents: from clinical concerns to recent Zn-alloys, Adv Healthc Mater 5 (10) (2016) 1121–1140.
[5] J. Venezuela, M.S. Dargusch, The influence of alloying and fabrication techniques on the mechanical properties, biodegradability and biocompatibility of zinc: a comprehensive review, Acta Biomater. 87 (2019) 1–40.
[6] H. Yang, X. Qu, W. Lin, C. Wang, D. Zhu, K. Dai, Y. Zheng, In vitro and in vivo studies on zinc-hydroxyapatite composites as novel biodegradable metal matrix composite for orthopedic applications, Acta Biomater. 71 (2018) 200–214.
[7] P.K. Bowen, J. Drelich, J. Goldman, Zinc exhibits ideal physiological corrosion behavior for bioabsorbable stents, Adv. Mater. 25 (18) (2013) 2577–2582.
[8] H. Yang, C. Wang, C. Liu, H. Chen, Y. Wu, J. Han, Z. Jia, W. Lin, D. Zhang, W. Li, W. Yuan, H. Guo, H. Li, G. Yang, D. Kong, D. Zhu, K. Takashima, L. Ruan, J. Nie, X. Li, Y. Zheng, Evolution of the degradation mechanism of pure zinc stent in the one-year study of rabbit abdominal aorta model, Biomaterials 145 (2017) 92–105.
[9] Y. Liu, Y. Zheng, X.H. Chen, J.A. Yang, H. Pan, D. Chen, L. Wang, J. Zhang, D. Zhu, S. Wu, K.W.K. Yeung, R.C. Zeng, Y. Han, S. Guan, Fundamental theory of biodegradable metals—definition, criteria, and design, Adv. Funct. Mater. 29 (18) (2019).
[10] D. Zhu, Y. Su, M.L. Young, J. Ma, Y. Zheng, L. Tang, Biological responses and mechanisms of human bone marrow mesenchymal stem cells to Zn and Mg biomaterials, ACS Appl. Mater. Interfaces 9 (33) (2017) 27453–27461.
[11] J. Fu, Y. Su, Y.X. Qin, Y. Zheng, Y. Wang, D. Zhu, Evolution of metallic cardiovascular stent materials: a comparative study among stainless steel, magnesium and zinc, Biomaterials 230 (2020) 119641.
[12] J. Ma, N. Zhao, L. Betts, D. Zhu, Bio-adaption between magnesium alloy stent and the blood vessel: a review, J. Mater. Sci. Technol. 32 (9) (2016) 815–826.
[13] J. Ma, N. Zhao, D. Zhu, Bioabsorbable zinc ion induced biphasic cellular responses in vascular smooth muscle cells, Sci. Rep. 6 (2016) 26661.
[14] J. Ma, N. Zhao, D. Zhu, Endothelial cellular responses to biodegradable metal zinc, ACS Biomater. Sci. Eng. 1 (11) (2015) 1174–1182.
[15] I. Cockerill, Y. Su, S. Sinha, Y.X. Qin, Y. Zheng, M.L. Young, D. Zhu, Porous zinc scaffolds for bone tissue engineering applications: a novel additive manufacturing and casting approach, Mater Sci Eng C Mater Biol Appl 110 (2020) 110738.
[16] G. Li, H. Yang, Y. Zheng, X.-H. Chen, J.-A. Yang, D. Zhu, L. Ruan, K. Takashima, Challenges in the use of zinc and its alloys as biodegradable metals: perspective from biomechanical compatibility, Acta Biomater. 97 (2019) 23–45.
[17] S. Zhao, C.T. McNamara, P.K. Bowen, N. Verhun, J.P. Braykovich, J. Goldman, J. W. Drelich, Structural characteristics and in vitro biodegradation of a novel Zn-Li alloy prepared by induction melting and hot rolling, Metall. Mater. Trans. 48 (3) (2017) 1204–1215.
[18] Z. Li, Z.-Z. Shi, Y. Hao, H.-F. Li, X.-F. Liu, A.A. Volinsky, H.-J. Zhang, L.-N. Wang, High-performance hot-warm rolled Zn-0.8Li alloy with nano-sized metastable precipitates and sub-micron grains for biodegradable stents, J. Mater. Sci. Technol. 35 (11) (2019) 2618–2624.
[19] S. Zhu, C. Wu, G. Li, Y. Zheng, J.-F. Nie, Creep properties of biodegradable Zn-0.1Li alloy at human body temperature: implications for its durability as stents, Materials Research Letters 7 (9) (2019) 347–353.
[20] Z. Li, Z.-Z. Shi, Y. Hao, H.-F. Li, H.-J. Zhang, X.-F. Liu, L.-N. Wang, Insight into role and mechanism of Li on the key aspects of biodegradable Zn Li alloys: microstructure evolution, mechanical properties, corrosion behavior and cytotoxicity, Mater. Sci. Eng. C 114 (2020).
[21] S. Zhu, C. Wu, G. Li, Y. Zheng, J.-F. Nie, Microstructure, mechanical properties and creep behaviour of extruded Zn-xLi (x = 0.1, 0.3 and 0.4) alloys for biodegradable vascular stent applications, Mater. Sci. Eng., A 777 (2020).
[22] Y. Zhang, Y. Lu, X. Xu, L. Chen, T. Xiao, X. Luo, Y. Yan, D. Li, Y. Dai, K. Yu, Microstructure, corrosion behaviors in different simulated body fluids and cytotoxicity of Zn–Li alloy as biodegradable material, Mater. Trans. 60 (4) (2019) 583–586.
[23] S. Zhao, J.M. Seitz, R. Eifler, H.J. Maier, R.J. Guillory 2nd, E.J. Earley, A. Drelich, J. Goldman, J.W. Drelich, Zn-Li alloy after extrusion and drawing: structural, mechanical characterization, and biodegradation in abdominal aorta of rat, Mater Sci Eng C Mater Biol Appl 76 (2017) 301–312.
[24] H. Yang, B. Jia, Z. Zhang, X. Qu, G. Li, W. Lin, D. Zhu, K. Dai, Y. Zheng, Alloying design of biodegradable zinc as promising bone implants for load-bearing applications, Nat. Commun. 11 (1) (2020) 401.
[25] G. Li, H. Yang, Y. Zheng, X.H. Chen, J.A. Yang, D. Zhu, L. Ruan, K. Takashima, Challenges in the use of zinc and its alloys as biodegradable metals: perspective from biomechanical compatibility, Acta Biomater. 97 (2019) 23–45.
[26] K. Torne, A. Ornberg, J. Weissenrieder, Influence of strain on the corrosion of magnesium alloys and zinc in physiological environments, Acta Biomater. 48 (2017) 541–550.
[27] B.S. Padekar, R.K. Singh Raman, V.S. Raja, L. Paul, Stress corrosion cracking of a recent rare-earth containing magnesium alloy, EV31A, and a common Al-containing alloy, AZ91E, Corrosion Science 71 (2013) 1–9.
[28] Y. Gao, L. Wang, L. Li, X. Gu, K. Zhang, J. Xia, Y. Fan, Effect of stress on corrosion of high-purity magnesium in vitro and in vivo, Acta Biomater. 83 (2019) 477–486.
[29] R. Abbaschian, L. Abbaschian, R.E. Reed-Hill, Physical Metallurgy Principles, fourth ed., Cengage Learning, Stamford, CT, 2010.
[30] H. Okamoto, Li-Zn (Lithium-Zinc), J. Phase Equilibria Diffus. 33 (4) (2012) 345, 345.
[31] C. Mao, Microstructure and Deformation Mechanism of Zn-Li Alloys, Chongqing University, 2018.
[32] V. Pavlyuk, I. Chumak, L. Akselrud, S. Lidin, H. Ehrenberg, LiZn(4 - x) (x = 0.825) as a (3 + 1)-dimensional modulated derivative of hexagonal close packing, Acta Crystallogr B Struct Sci Cryst Eng Mater 70 (Pt 2) (2014) 212–217.
[33] M.E. Kassner, T.A. Hayes, Creep cavitation in metals, Int. J. Plast. 19 (10) (2003) 1715–1748.
[34] S.P. Lynch, 1 - mechanistic and fractographic aspects of stress-corrosion cracking (SCC), in: V.S. Raja, T. Shoji (Eds.), Stress Corrosion Cracking, Woodhead Publishing2011, pp. 3-89.
[35] W. Dietzel, P. Bala Srinivasan, A. Atrens, 3 - testing and evaluation methods for stress corrosion cracking (SCC) in metals, in: V.S. Raja, T. Shoji (Eds.), Stress Corrosion Cracking, Woodhead Publishing, 2011, pp. 133–166.
[36] M. Bobby Kannan, R.K. Singh Raman, Evaluating the stress corrosion cracking susceptibility of Mg–Al–Zn alloy in modified-simulated body fluid for orthopaedic implant application, Scripta Mater. 59 (2) (2008) 175–178.
[37] A. Oyane, H.-M. Kim, T. Furuya, T. Kokubo, T. Miyazaki, T. Nakamura, Preparation and assessment of revised simulated body fluids 65A (2) (2003) 188–195.
[38] N. Winzer, A. Atrens, G. Song, E. Ghali, W. Dietzel, K.U. Kainer, N. Hort, C. Blawert, A critical review of the stress corrosion cracking (SCC) of magnesium alloys, Adv. Eng. Mater. 7 (8) (2005) 659–693.
[39] K. Chen, Y. Lu, H. Tang, Y. Gao, F. Zhao, X. Gu, Y. Fan, Effect of strain on degradation behaviors of WE43, Fe and Zn wires, Acta Biomater. (2020).